

Correspondence to: Peter Dalin (pdalin@irf.se)

1 Introduction

Noctilucent clouds (NLC) are the highest clouds in the Earth's atmosphere, forming in the summer mesopause region between 80 and 90 km altitude at middle and polar latitudes in both hemispheres. They consist of water-ice particles with radii of 30–100 nm that scatter sunlight, making the clouds visible against the twilight sky. NLCs are typically observed from May to September in the Northern Hemisphere and from November to February in the Southern Hemisphere (Gadsden and Schröder, 1989; Liu et al., 2016). When observed from space, these clouds are traditionally called Polar Mesospheric Clouds (PMC) (Thomas, 1984).



NLC and PMC are systematically studied using ground-based optical cameras, spectrographs, lidars as well as dedicated spaceborne instruments (e.g., Karlsson and Gumbel, 2005; Dalin et al., 2008; Bailey et al., 2009; Fiedler et al., 2011; DeLand and Thomas, 2015; Tsuda et al., 2022; Wallis et al., 2025). In addition, irregular campaign-based NLC observations are carried out using sounding rockets and aircraft (Zadorozhny et al., 1993; Gumbel and Witt, 2001; Reimuller et al., 2011; Suzuki et al., 2022; Pertsev et al., 2024). Each observational technique has specific advantages and limitations. In particular, ground-based imagers offer high horizontal (~20 m) and temporal (~1 s) resolution (Dalin et al., 2010; Baumgarten and Fritts, 2014), and lidars provide high vertical resolution (50–150 m; Baumgarten et al., 2009), but both are restricted by tropospheric weather and limited geographic coverage. Conversely, satellite observations deliver global PMC coverage but suffer from low spatial (~1 km) and temporal (minutes to hours) resolution. Moreover, sun-synchronous satellites introduce large spatial gaps (hundreds of km) between adjacent orbits at mid- and subpolar latitudes (45–60°N) due to a spacecraft orbiting the Earth. Consequently, no single existing technique can fully resolve the microphysical and dynamical processes governing NLC/PMC.

Balloon-borne observations from stratospheric altitudes (25–40 km) have a potential for comprehensive studies of NLC on a regular basis. Such observations provide several advantages: independence from tropospheric weather, uninterrupted 24 h coverage, and proximity to the NLC layer (80–85 km), yielding the highest achievable spatial resolution. From this vantage point, both large-scale (up to 2500 km, limited by Earth’s curvature) and small-scale (down to meters) NLC features can be observed. Furthermore, balloon-borne observations at 30–40 km altitude occur above the ozone-rich layer (20–25 km), thereby avoiding light absorption in the Chappuis band (400–650 nm).

To date, four balloon-borne experiments have been dedicated to NLC observations from the stratosphere (Miller et al., 2015; Dalin et al., 2019, 2020, 2022; Fritts et al., 2019). These missions have provided unique datasets for studying both large- and small-scale wave dynamics and turbulence within NLC layers. In this study, we present results from a new long-duration balloon experiment aimed at investigating NLC in the polar mesopause. We describe the observation technique and instrumentation as well as early scientific findings. The stratospheric NLC observations were complemented by ground-based lidars and, for the first time, by spaceborne measurements from the Swedish MATS satellite. Additionally, temperature and water vapor data from the Aura/MLS satellite were used to characterize the mesopause environment during the TRANSAT flight, and JAWARA model data were employed to simulate the thermodynamic and wind conditions in support of the NLC observations.

68

69 **2 Technique and method**

70 **2.1 Technical characteristics of the imager**

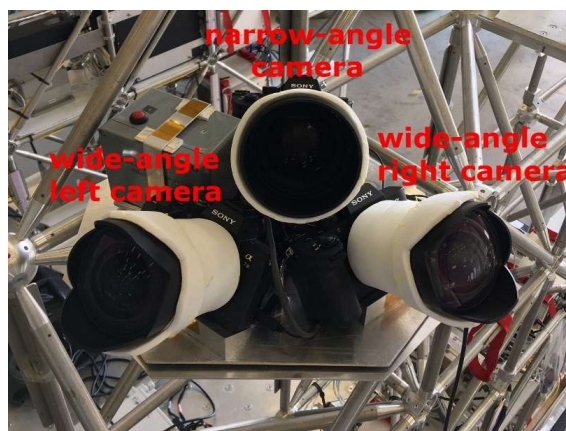
The Stratospheric Observations of Noctilucent Clouds (SONC) experiment is a balloon-borne scientific mission designed to investigate NLC dynamics across a broad range of spatial scales—from large-scale structures (30–2500 km) to fine-scale features (5 m–30 km)—as well as the microphysical properties of NLC ice particles.

To achieve these objectives, three high-resolution, high-sensitivity Sony $\alpha 7$ Mark III cameras were used. Each camera has a full-frame 35 mm, 24-megapixel sensor (6000×4000 pixels). Two cameras were equipped with wide-angle lenses (field of view, FoV, = $105.4^\circ \times 81.8^\circ$), while the third carried a narrow-angle lens

77



78 (FoV=15.0° × 10.1°). This configuration, two wide-angle and one narrow-angle camera, provides a horizontal
 79 coverage of about 180° for studying mesospheric NLC structures up to 2500 km across, while simultaneously
 80 enabling spatial resolution as fine as about 5 m when viewing the NLC layer at 83 km from a 40 km altitude and
 81 35° elevation angle. Note that such simultaneous access to both large and small scales is currently unattainable
 82 from either ground-based or satellite platforms. The three cameras formed the SONC imager, illustrated in Fig.
 83 1. Each camera stored data on two 1 TB SD cards. Given the expected 4–5 day duration of the transatlantic flight
 84 and the storage limits, an image acquisition cadence of 50 s was chosen. This temporal resolution enables
 85 tracking the evolution of small-scale wave activity within the NLC layer as well as monitoring large-scale cloud
 86 dynamics. The optical axes of the two wide-angle cameras were inclined at 36° to the horizontal plane in order to
 87 minimize light contamination from bright tropospheric scattering and from above coming from a big white
 88 balloon envelope (~70 m in diameter). The narrow-angle camera was tilted at 35° to the horizontal plane to
 89 resolve fine-scale structures of NLC.



90
 91 **Figure 1: The SONC imager consists of three Sony α7 Mark III cameras and the electronic control unit**
 92 **(gray box with red button). Two cameras are equipped with wide-angle lenses, and one with a narrow-**
 93 **angle lens positioned between them. The instrument was used to observe noctilucent clouds during the**
 94 **TRANSAT transatlantic balloon flight (22–26 June 2024).**

95
 96 Automatic exposure bracketing was applied, capturing 5 images sequentially with exposure times varying
 97 between 1/1600 s and 1.6 s. This approach accommodated a wide dynamic range of NLC brightness under
 98 variable atmospheric background illumination conditions. One wide-angle camera (left in Fig. 1) operated
 99 flawlessly throughout the 3.8-day flight, producing a total of about 40,000 images. The other wide-angle and the
 100 narrow-angle cameras functioned for the first 13 h and 12 h, respectively, before ceasing operation for unknown
 101 reasons. The imager survived the gondola landing on the ice of Baffin Island without damage. Post-flight tests of
 102 all the cameras and electronics confirmed full functionality of the SONC imager and no performance
 103 degradation.

104 2.2 Technical characteristics of the TRANSAT balloon flight



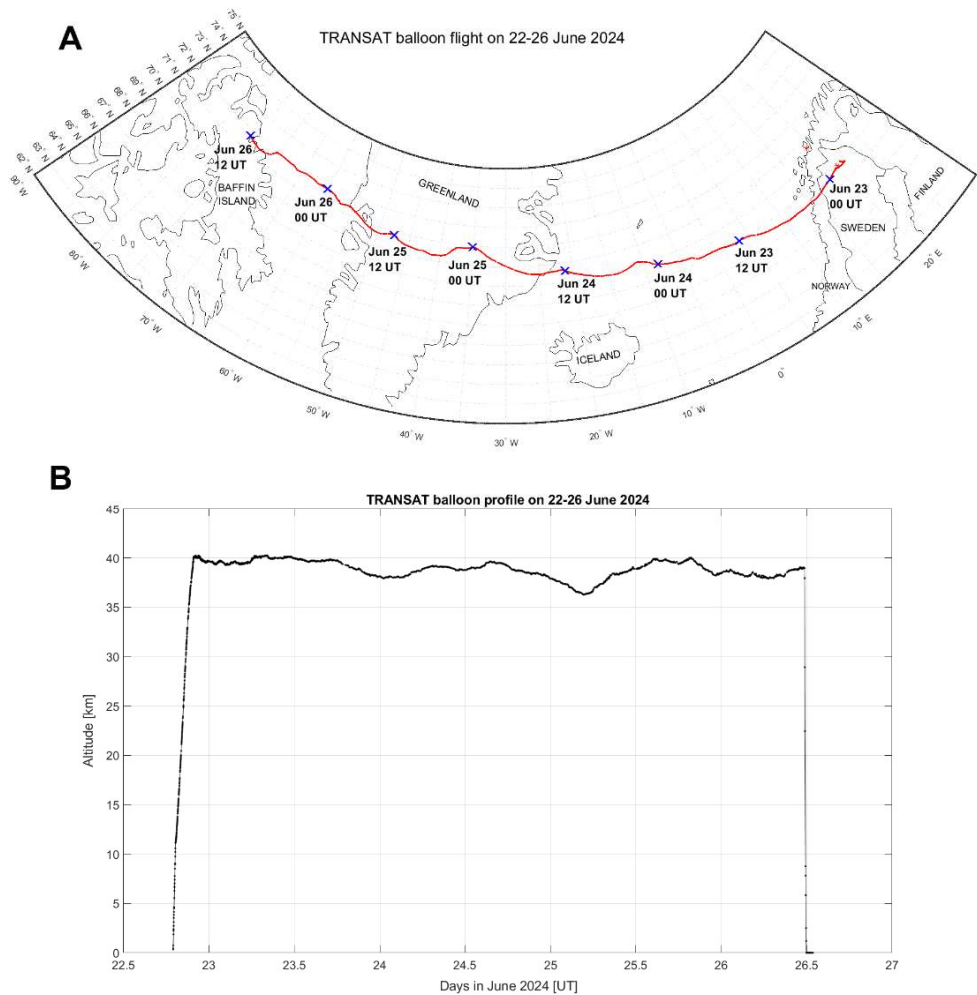
106 The TRANSAT mission is a long-duration stratospheric balloon flight organized and operated by the French
107 Space Agency (CNES) (<https://cnes.fr/en/news/balloons-crossing-atlantic-wind>) for multidisciplinary
108 atmospheric and cosmic research. The gondola, named Carmen, had a total mass of about 900 kg and carried
109 nine scientific instruments. Two of these were from Sweden: the SONC imager and an infrasound instrument
110 dedicated to studies of infrasound atmospheric waves and their sources. The infrasound experiment and its
111 scientific results will be described in a separate paper.

112 The Carmen gondola utilized a three-axis motorized gimbal stabilized platform, providing an elevation-angle
113 stability of 0.15° , an absolute azimuth pointing accuracy of 1° and a stability of ± 10 arcmin around it. Because
114 stratospheric balloons rotate continuously, such stabilization was critical to avoid image smearing and to
115 maintain consistent NLC monitoring at fine and large scales.

116 As the transatlantic flight took place under solstice conditions with continuous solar illumination, scientific
117 instruments were mounted behind a solar shield to prevent overheating and stray-light interference. To ensure
118 continuous shading, the gondola was slowly rotated to keep the solar shield facing the Sun throughout the flight.

119 The TRANSAT balloon was launched from Esrange, northern Sweden (67.89° N, 21.08° E) at 18:57 UTC
120 (20:57 LT) on 22 June 2024 and landed on Baffin Island, northern Canada, at 12:14 UTC (08:14 LT) on 26 June
121 2024. The total flight time was about 90 h (3.8 days), with an average horizontal speed of about 11 m s^{-1} . The
122 horizontal trajectory and altitude profiles of the TRANSAT mission are shown in Fig. 2.

123



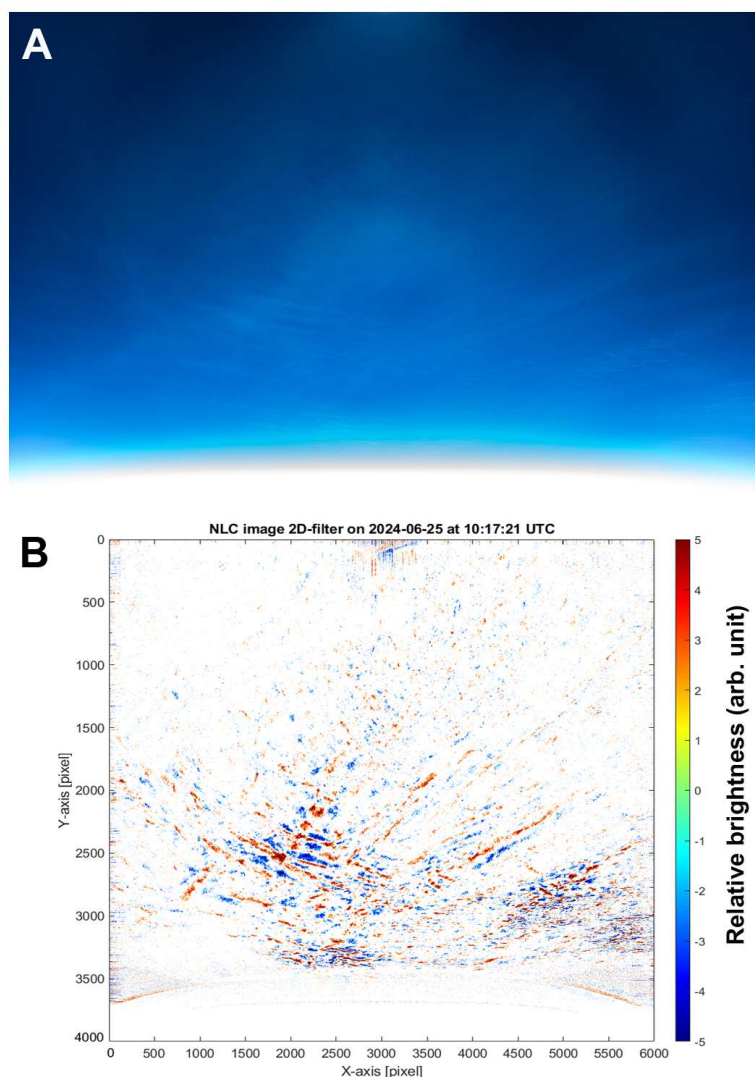
124
125 **Figure 2: (A) Horizontal trajectory (the red line) of the TRANSAT balloon mission between 22 and 26**
126 **June 2024. The blue crosses mark the balloon’s position every 12 h. (B) Altitude profile of the TRANSAT**
127 **flight.**

128
129 **2.3 Image processing**

130 Prior to launch, all three Sony cameras underwent geometrical calibration on the ground using night-sky
131 images containing reference stars. A second-order polynomial camera model was fitted by comparing theoretical
132 and measured horizontal coordinates for over 200 identified reference stars. Six free coefficients describing focal
133 length, image orientation, and optical distortion were determined. These coefficients were used to compute
134 relative horizontal coordinates (elevation and azimuth angles relative to the center of the image) for every pixel
135 of each camera.



136 Given the known position and orientation of the SONC imager within the gondola reference frame, provided
137 by CNES, the absolute horizontal coordinates of all pixels were computed. Subsequently, a georeferencing
138 procedure projected each pixel onto the Earth's surface, assuming a mean NLC altitude of 83 km. Details of the
139 calibration, georeferencing, and error analysis are available in Dalin et al. (2015).
140 NLC identification was performed using both manual and automatic approaches. In the manual procedure, about
141 6200 images, suitable for scientific analysis, from the left camera (Fig. 1) were carefully examined to mark NLC
142 presence or absence. The number of images is 6200 because almost every image in a series of 5 images, taken in
143 bracketing mode, was analyzed. A video sequence was then assembled to verify temporal continuity. This video,
144 containing all images with synchronized flight parameters, timestamps and balloon coordinates, is available at
145 the Harvard Dataverse repository (<https://doi.org/10.7910/DVN/1PHRZU>).
146 Automatic image processing involved several steps: (1) Background subtraction: A second-order polynomial
147 fit was used to estimate the sky background along each vertical column of pixels, which was then subtracted to
148 yield a residual brightness of each pixel. (2) Two-dimensional Fourier filtering: applied to a residual brightness
149 to extract gravity-wave-like patterns on image (see Fig. 3b). (3) Wavelet analysis: a Morse analytic wavelet
150 transform was applied to selected images to quantify horizontal wavelengths of identified wave patterns. Each
151 image was first projected onto Earth geographical coordinates (in km) prior to the analysis. An example (Fig. 4)
152 shows dominant horizontal wavelengths of about 30 and 40 km, which are frequently observed in NLC (Pautet et
153 al., 2011; Demissie et al., 2014).
154



155
 156 **Figure 3: (A) Example of NLC image acquired at 10:17:21 UTC on 25 June 2024 during the TRANSAT**
 157 **balloon flight. (B) Two-dimensional Fourier-filtered version of (A), highlighting residual brightness**
 158 **variations associated with NLC bands seen in the middle and the lower part of the image.**
 159

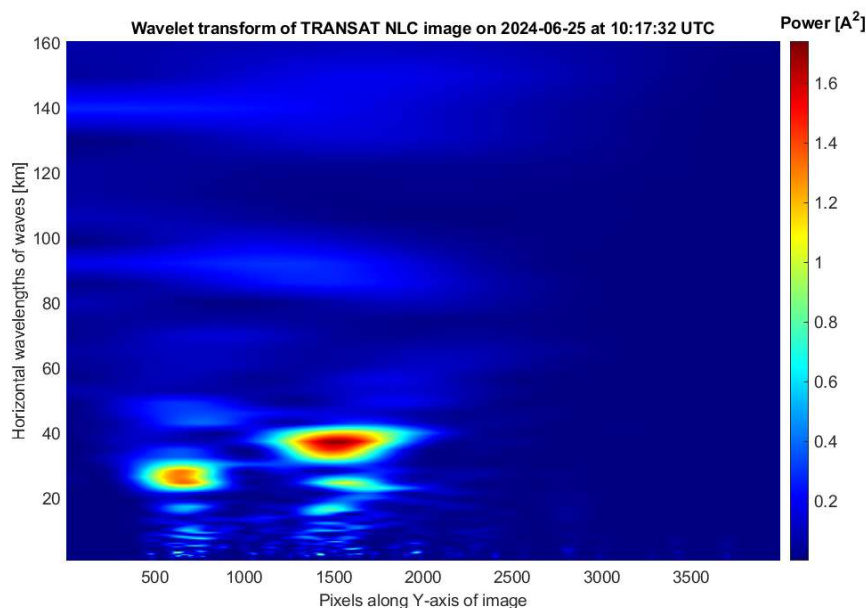


Figure 4: Example of a wavelet transform for the NLC image obtained at 10:17:21 UTC on 25 June 2024 during the TRANSAT flight. Gravity waves having prevailing horizontal scales of about 30 and 40 km are clearly seen as the red color code.

4) A keogram representation of a sequence of all analyzed images helps to identify the presence or absence of NLC as a function of time. Keogram is a slice of an image along a specific axis, and many such slices are put together as a function of time to produce brightness variations of an observed atmospheric phenomenon over time. Keogram is commonly used to demonstrate a presence or absence of aurora in all-sky images. In the present study, based on the manual careful inspection of 6200 images suitable for scientific analysis, we have selected horizontal pixel lines in the range of 3000-3400 pixels (counting along the Y-axis from the top of the image) at which NLC preferred to appear. The image coordinates are present in Fig. 3b. These pixels were summed to produce an integrated brightness for every column between 3000 and 3400 pixels. The mean value and its standard deviation (std) were then calculated for the given slice along the X-axis of the image. Next, a selection rule was applied: brightness values greater than 1 std of the mean were selected to classify the given slice as NLC present or absent. Then keogram was created by putting together slices of about 6200 images (Fig. 5), demonstrating nearly continuous presence of NLC, that is discussed in detail in Section 4. This automatic keogram procedure fits well with the manual procedure (described above) in identifying the presence or absence of NLC as a function of time.

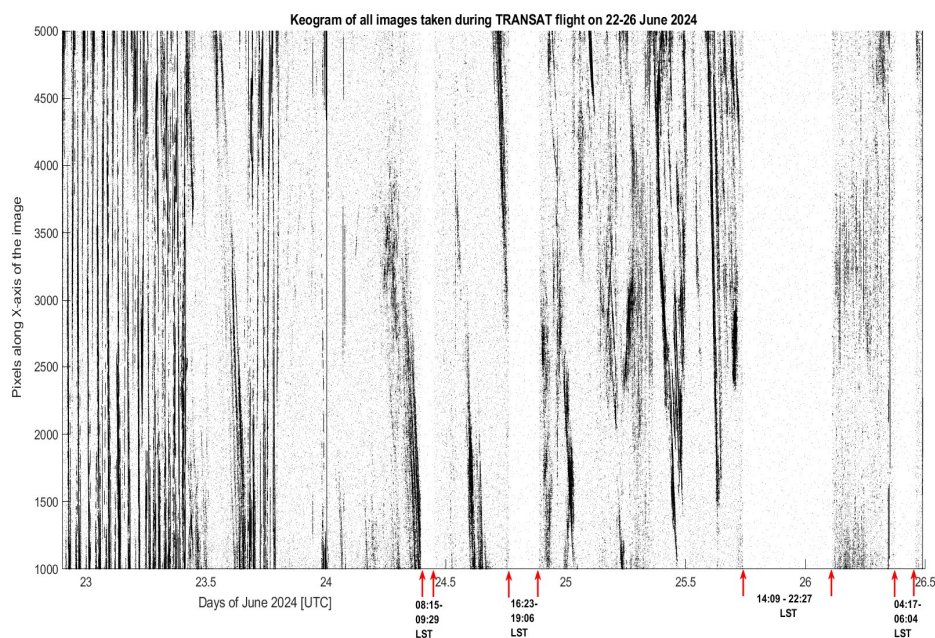


Figure 5: Keogram compiled from about 6200 images during the TRANSAT balloon flight on 22-26 June 2024. The red arrows mark four time intervals (white-grey areas) when NLC were absent. Corresponding local solar times (LST) are shown for four time intervals on the x-axis.

3 Ground-based and space complementary measurements

3.1 Lidar measurements

During the initial phase of the TRANSAT balloon flight, complementary lidar measurements were performed at Esrang (67.8°N, 21.1°E, Sweden) and Andøya (69.3°N, 16.0°E, Norway), with the aim to provide simultaneous and common volume (or in proximity) measurements of NLC layers above northern Scandinavia. At Esrang, we use a Rayleigh/Mie/Raman (RMR) backscatter lidar developed by the Bonn University to monitor aerosols in the troposphere, stratosphere and mesosphere as well as to determine temperature profiles in the aerosol-free part of the atmosphere (Blum and Fricke, 2005). The vertical and time resolution of the obtained measurements by the Esrang lidar is 150 m and 4.4 min, respectively. At Andøya, we use an RMR-lidar which has been operated as part of the Arctic Lidar Observatory for Middle Atmosphere Research (ALOMAR). Using measurements of the ALOMAR lidar one can study temperatures and winds in the middle atmosphere, aerosol layers in the stratosphere, polar stratospheric clouds in the lower stratosphere in winter and noctilucent clouds in the mesopause region in summer (Baumgarten, 2010). We use lidars backscattered signals from the 532-nm wavelength channel to measure NLC over Esrang and Andøya during the TRANSAT flight in the stratosphere over northern Scandinavia. The vertical and time resolution of the obtained measurements by the ALOMAR lidar is 40 m and 30 s, respectively.

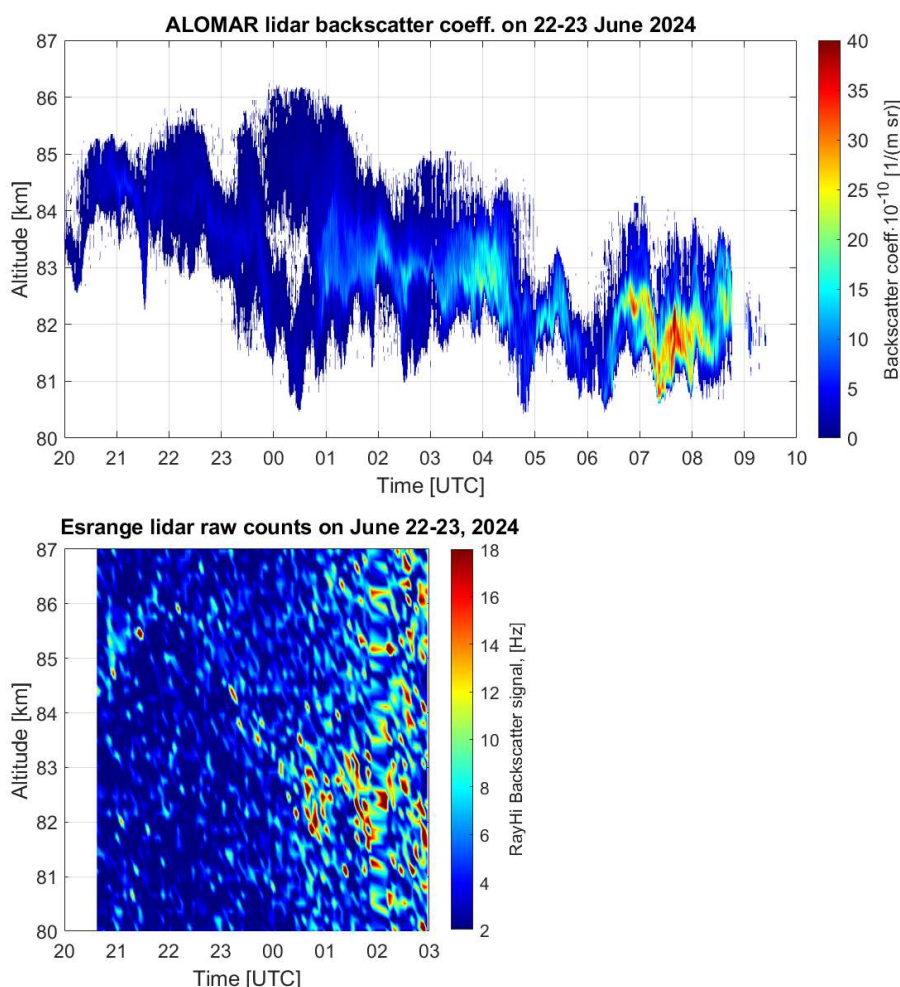


Figure 6: Lidar measurements at Andøya, Norway (upper panel) and Esrange, Sweden (lower panel) during the initial phase of the TRANSAT balloon flight on 22-23 June 2024.

The results of the lidar measurements during the initial phase of the TRANSAT flight are shown in Fig. 6. The NLC layer is clearly seen in both lidar measurements between 81 and 86 km altitude. Between 20 and 22 UTC, the NLC layer lifted up from 84 to 86 km, then it sank to 81-82 km between 22 UTC on 22 June and 01 UTC on 23 June as demonstrated by both lidars. Note that the ALOMAR lidar registered a double-layer NLC structure between 00 and 01 UTC. Another double-layer NLC structure will be discussed in section 4. These height variations of the NLC layer are due to propagating atmospheric gravity waves and turbulent vorticities. Note that it is a very rare case of conducting simultaneous lidar measurements at Andøya and Esrange (separated by ~250 km) on both sides of the Scandinavian range, registering about the same NLC layer. After 01 UTC, Esrange lidar measurements become too noisy to distinguish the NLC signal from noise. The ALOMAR lidar operated until 12 UTC on 23 June, continuously registering the enhanced NLC layer until 09 UTC, with height



215 variations between 81 and 84 km. The extended NLC field was registered from the stratosphere above northern
 216 Scandinavia (not shown in figure) shortly after the TRANSAT balloon launch and during the lidar measurements,
 217 thus continuously observing nearly the same NLC layer from the ground and stratosphere from evening hours on
 218 22 June until morning hours on 23 June. Thus, lidar measurements complement balloon-borne observations,
 219 providing information on vertical dynamics of the NLC layer observed from the stratosphere.

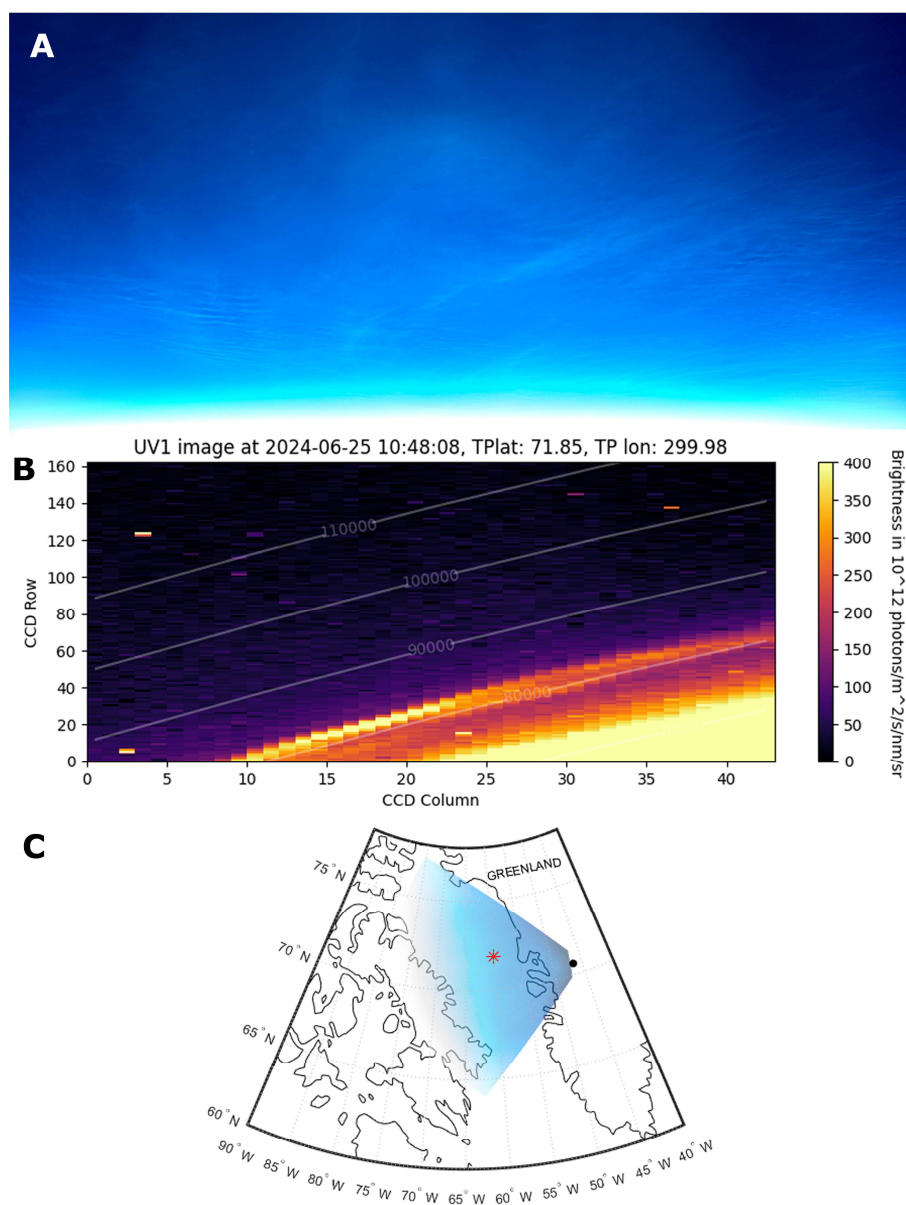
220

221 3.2 Space measurements

222 During the TRANSAT flight, measurements of PMC from space were also conducted with the MATS
 223 satellite. MATS (Mesospheric Airglow/Aerosol Tomography and Spectroscopy) is a Swedish satellite mission,
 224 launched in November 2022, designed to investigate polar mesospheric clouds, temperature regime and
 225 atmospheric gravity waves in the mesosphere (Gumbel et al., 2020). The MATS satellite utilizes airglow
 226 emissions coming from excited molecular oxygen in the near infrared range of the spectrum (760-780 nm, the O₂
 227 (0-0) A-band) as well as scattered light from PMC in the ultraviolet (270 and 340 nm). The primary scientific
 228 instrument on-board the satellite is the limb imager, a telescope with 6 wavelength channels that continuously
 229 captures high-resolution images of the atmospheric limb with a field of view of about 40 km in the vertical and
 230 250 km across track at the tangent point. Using a tomographic analysis of acquired MATS images, one can
 231 reconstruct waves in three dimensions and provide 3-dimensional fields of airglow, PMC properties and
 232 temperature (Megner et al., 2025).

233 Figure 7 demonstrates an example of MATS images in the UV channel 1 at 270 nm taken at 10:48:08 UTC
 234 on 25 June 2024. This measurement was done at the tangent point in the mesopause close to the west coast of
 235 Greenland as illustrated in Fig. 7c. One can clearly see the presence of the PMC layer in Fig. 7b as the bright
 236 yellow band on the atmospheric limb between 80 and 85 km tangent altitude. The time and location of the PMC
 237 by MATS agree very well (time difference of 6 seconds) with the NLC observation obtained from the
 238 stratosphere, with the MATS tangent point being in the field of view of the SONC imager as seen in Fig 7c. Such
 239 simultaneous common-volume observation of NLC from the stratosphere and space was made for the second
 240 time; the first one was made by the PMC Turbo stratospheric flight and the AIM satellite in July 2018 (Fritts et
 241 al., 2019). But in the present study this was done for the first time when such a large-scale NLC/PMC field
 242 (extending at least 1500 km from north to south) was seen from the stratosphere and from space based on the
 243 limb-viewing observation using the MATS satellite. It should also be noted that MATS registered the PMC layer
 244 before and after the time shown in Fig. 7, i.e., MATS observed an extended PMC layer in a large volume of the
 245 mesopause at least over Greenland, Baffin Bay and Baffin Island. Part of this large-scale NLC field was
 246 registered from the stratosphere by the SONC imager. At the same time, images taken from the stratosphere have
 247 much higher spatial resolution, showing small- and medium-scale wave dynamics (including smaller gravity
 248 waves and turbulent structures) that MATS cannot resolve using the limb-viewing geometry. Thus, studies of
 249 spatial-temporal variability of NLC/PMC can be carried out simultaneously from the stratosphere and space,
 250 complementing each other.

251



252
 253 **Figure 7: Example of NLC measurements obtained from the stratosphere and space on 25 June 2024**
 254 **during the TRANSAT balloon flight. (A) Image, taken by the SONC imager from the stratosphere at**
 255 **10:48:02 UTC, shows the extended NLC field covering almost the whole image area. (B) Image, taken by**
 256 **the MATS satellite at 10:48:08 UTC, illustrate part of the atmospheric limb, with the bright yellow PMC**
 257 **layer seen between 80 and 85 km. Data are shown for the UV channel 1 at 270 nm. (C) Projection of the**
 258 **NLC image shown on Panel A onto the Earth's surface. The black dot is the position of the TRANSAT**
 259 **balloon, the red asterisk marks the MATS tangent point which is in the field of view of the SONC imager.**
 260



4 Results and Discussion

4.1 Nearly continuous observations of NLC

The first unexpected scientific result is the nearly continuous presence of mesospheric clouds during 3.8 days of the TRANSAT balloon flight. In total, there were four intervals of NLC disappearances as shown by the red arrows in Fig. 5. These events occurred on 23 June at 09:30–10:50 UTC on 23 June, at 18:20–21:20 UTC on 24 June, at 17:45–02:40 UTC on 25–26 June, and at 09:00–11:00 UTC on 26 June. Outside these intervals, NLC were continuously observed, often with varying brightness and wave modulation.

These NLC disappearances are not related to local solar time (see four local solar time intervals on the x-axis in Fig. 5). That is, these NLC interruptions were of a rather spontaneous nature and were not related to solar thermal tides, which are regular atmospheric variations. Indeed, Fritts et al. (2019) demonstrated more or less regular NLC disappearances in the evening (18–24 LST) and morning hours (6–12 LST), observed during the PMC Turbo balloon flight from Sweden to Canada in July 2018. The authors associated this with solar semidiurnal and diurnal thermal tides in the polar summer mesopause, the amplitudes of which reach 10–20 K, which is comparable to ones by gravity waves in the mesopause region (Rapp et al., 2002). It should be noted that this result was obtained on the basis of lidar measurements on the PMC Turbo balloon, that is, obtained with a very small field of view of a few meters in the mesopause. Therefore, for such a small volume of the mesopause one can expect the dominant influence of large-scale waves such as solar tides. In the case of the TRANSAT balloon flight NLC observations were carried out on large scales of about 1000–1500 km at a time. At such large scales, not only solar tides manifest themselves but also propagating gravity waves of various scales from 1 to 1000 km. Indeed, a typical picture seen from the stratosphere was that we saw a disappearance of NLC in one area of the mesopause (for example, in the eastern part), but simultaneous appearance of other NLC in another part of the mesopause (for example, in the western part). In other words, large-scale NLC fields were generally represented by numerous wavy patterns of sporadic nature. One can assume that gravity waves, continuously coming from the lower atmosphere, form a new NLC and/or modulate an existing NLC layer in different parts of the mesopause (as observed in the present experiment), thereby dominating solar thermal tides on large scales. At the same time, we should note that this result was obtained on the basis of a single 3.8-day flight and a limited range of latitudes (60–75°N) and longitudes (45°E–95°W). That is why the present case study cannot claim to be a general statement about the relative importance of solar tides compared to gravity waves.

4.2 A case study of the NLC disappearance

The second result is connected to the disappearance of NLC at 18:20–21:20 UTC (16:23–19:06 LST) on 24 June 2024 (Fig. 5). This NLC disappearance was observed over the Atlantic Ocean near the east coast of Greenland and over Iceland as demonstrated in Fig. 8.

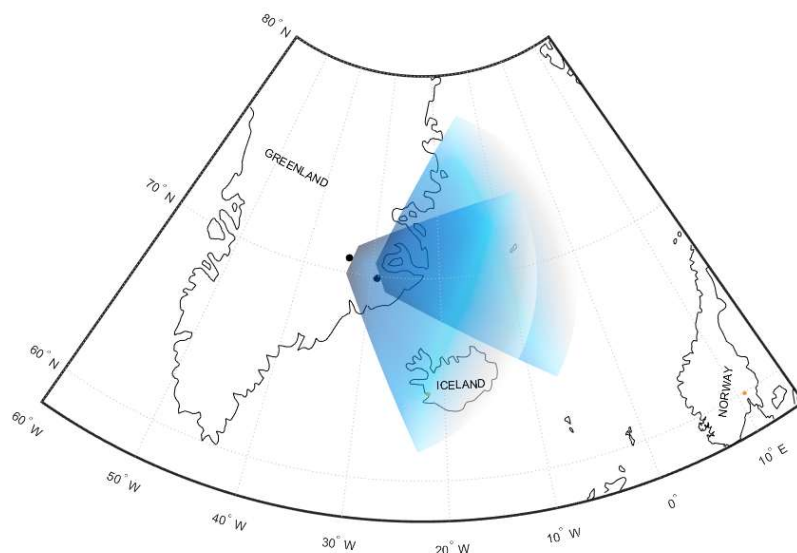


Figure 8: Projection of the field of view of the SONC camera on the Earth's surface at 18:20 UTC (16:23 LST) and 21:20 UTC (19:06 LST) on 24 June 2024, when no NLC were observed from the stratosphere. The black dots mark the position of the TRANSAT balloon.

We have tried to find out the reason for this NLC disappearance. For this data of the Aura/MLS temperature and water vapor measurements have been used to obtain a comprehensive picture of the mesopause environment in the region of interest. Aura/MLS temperature and water vapor measurements of ver.5.0 and level 2 data quality were obtained from the NASA public web-site: https://acdisc.gesdisc.eosdis.nasa.gov/data/Aura_MLS_Level2/. According to the Aura/MLS data quality and description document (version 5.0x level 2 and 3), for Aura/MLS temperature measurements, the vertical resolution in the mesopause region is 11 km at 0.01 hPa (~80 km) and 12 km at 0.001 hPa (~90 km). The horizontal resolution (along track) is ~250 km at 0.01 hPa and ~280 km at 0.001 hPa. The pressure range recommended for scientific use is from 261 hPa (~10 km) to 0.00046 hPa (~93 km). Typical precisions for individual Aura/MLS temperature profiles at this altitude range are ± 3.4 – 3.6 K. For Aura/MLS water vapor measurements, the vertical resolution is 8.8 km at 0.01 hPa and 10.3 km at 0.002 hPa. The horizontal resolution is ~725 km at 0.01 hPa and ~350 km at 0.002 hPa. The pressure range recommended for scientific use is from 316 hPa to 0.001 hPa. Typical precisions for individual Aura/MLS water vapor profiles are 55% at 0.01 hPa and 450% at 0.001 hPa. The description on the MLS temperature product and its validation can be found in



313 Froidevaux et al. (2006) and Schwartz et al. (2008). The validation of water vapor data is described in detail by
314 Read et al. (2007) and Lambert et al. (2007). The frost point temperature in the mesopause was calculated using
315 Aura/MLS water vapor data based on thermodynamics of the vapor pressure of ice (Murphy and Koop, 2005).
316 The results are shown in Fig. 9 demonstrating the following peculiar feature. A prominent localized warm
317 area in the mesopause region at the pressure levels of 0.0022 hPa (about 86 km geometrical height) and 0.0046
318 hPa (about 83 km) was present between Greenland and Scandinavia, with temperatures 20-30 K higher than
319 those in the adjacent mesopause regions at 0.0022 hPa. The location of this warm spot coincides well with the
320 position of the mesopause visible from the TRANSAT balloon when no NLC were seen (Fig. 8). The right
321 column in Fig. 9 shows the differences between the actual temperature measurements and the frost point
322 temperature as calculated using Aura/MLS water vapor measurements, with positive temperature differences
323 being as much as 10-15 K in the center of this warm spot. We double-checked all the Aura/MLS data
324 (temperature and water vapor) which show good quality data suitable for scientific analysis and we could not
325 find any error in these data.
326

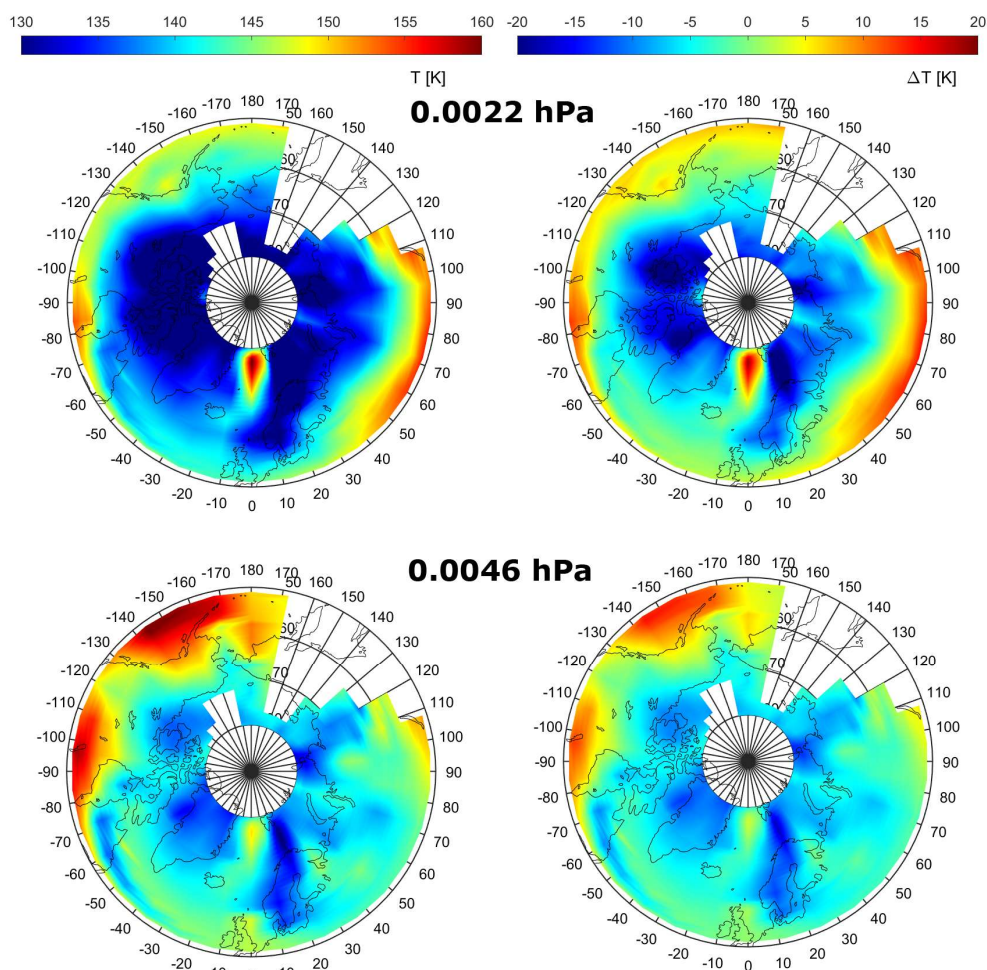


Figure 9: (Left column) Aura/MLS temperature measurements at the pressure level of 0.0022 hPa (~86 km) and at 0.0046 hPa (~83 km) on 24 June 2024. (Right column) Differences between the temperature and the frost point temperature as estimated based on Aura/MLS water vapor measurements at 0.0022 hPa and 0.0046 hPa (see the text).

In Fig. 9 (especially in plots for the 0.0046 hPa level), one can note that the warm local region at high latitudes was an extension of a warm vast area located at mid-latitudes. That is, one can assume that this local warm region was caused by a jet of warm air mass from middle latitudes to high latitudes. To test this hypothesis, we apply the Japanese Atmospheric General circulation model for Upper Atmosphere Research Data Assimilation System (JAGUAR-DAS), which is a data assimilation system for the whole neutral atmosphere (Koshin et al., 2020; 2022). Specifically, JAGUAR-DAS Whole neutral Atmosphere Reanalysis (JAWARA) has been considered in the present study. JAWARA is a long-period reanalysis, starting from September 2004, which covers the altitude range from the surface to the lower thermosphere (~110 km). The vertical resolution of



341 JAWARA data in the mesopause region between 80 and 90 km is about 0.7 km. JAWARA outputs, distributed
342 on a horizontal grid spacing of 2.81° , include the following hourly data: temperature, zonal, meridional and
343 vertical wind velocities, geopotential height, temperature tendency due to diabatic heating, zonal and meridional
344 forcing from the GW parameterization (Koshin et al., 2025). Note that JAWARA assimilates MLS temperature,
345 meaning that the temperature fields in MLS and JAWARA are not fully independent and the mutual agreement
346 might be expected because of the data assimilation.

347 JAWARA temperature and neutral wind data in the mesopause region are shown on 24 June 2024 in Fig. 10,
348 demonstrating the following features. The warm localized spot was present between Greenland and Scandinavia,
349 and it was most pronounced at 0.0042 hPa, ~ 83 km, (lower plots), which agrees well with the position of the
350 warm spot represented by Aura/MLS. At the same time, wind velocity vectors show that the local wind jet was
351 formed, which moved from middle to high latitudes in the region with this warm spot. Thus, this warm spot in
352 the mesopause was caused by the intrusion of a warm air mass from the middle to high latitudes between
353 Greenland and Scandinavia. This warm spot induced sublimation of ice particles in the mesopause, which caused
354 NLC to disappear during the TRANSAN balloon flight over the North Atlantic and the east coast of Greenland
355 in the evening of 24 June 2024. The mechanism of this air intrusion from middle to high latitudes is beyond the
356 scope of the present paper.

357

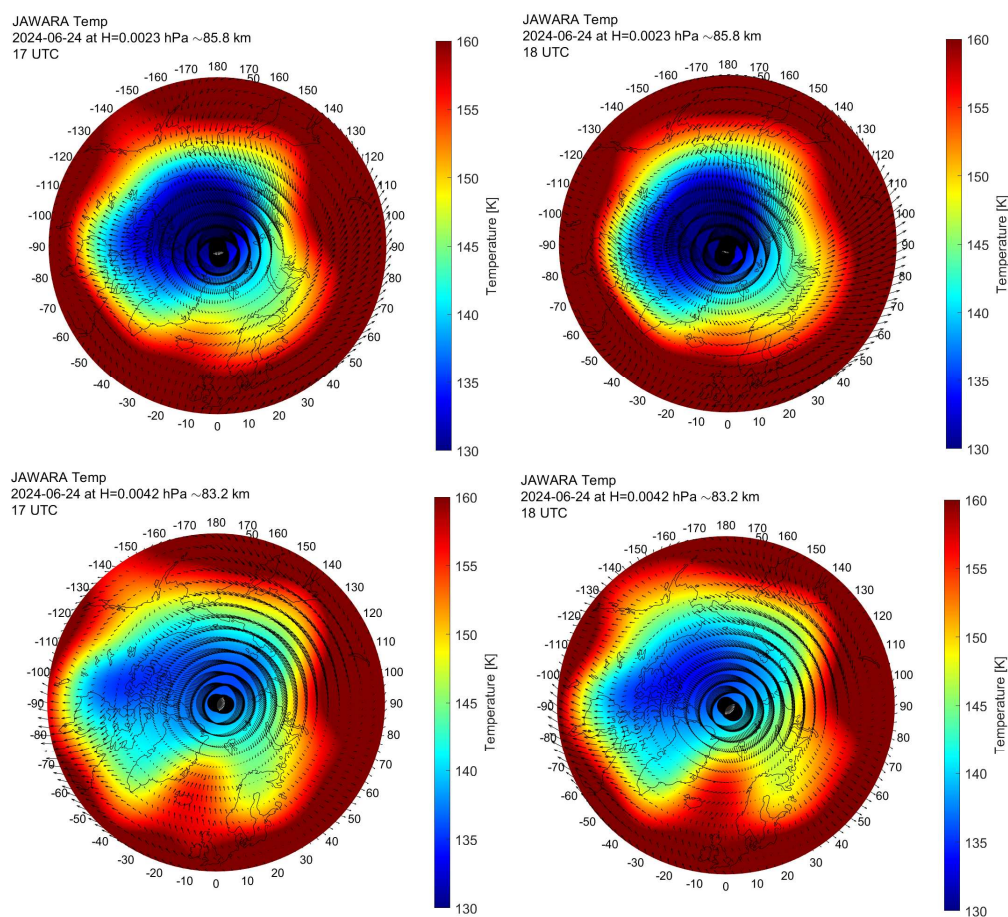


Figure 10: JAWARA model temperature (color code) and neutral wind velocity vectors (arrows) on 24 June 2024. The data are shown at the pressure level of 0.0023 hPa (upper panels) and at 0.0042 hPa (lower panels), and at 17:00 UTC (left column) and at 18:00 UTC (right column).

4.3 A double-layer structure in NLC

The third early result addresses a double-layer event in NLC observed over Greenland on 25 June 2024. The reader is recommended to look at the video of NLC image sequence at 05:08-06:49 UTC (02:35-04:08 LST) on 25 June (<https://doi.org/10.7910/DVN/AKJK4P>). One can see at least two NLC layers moving in opposite directions: one cloud layer visually moved approximately from the top to the bottom of the image frame, whereas another cloud layer moved in the opposite direction from the bottom to the top. Double-layer and multiple-layer structures in NLC/PMC have been previously observed and modeled in a number of studies (Baumgarten et al., 2012; Dubinskii and Popel, 2012; Kaifler et al., 2013; Gao et al., 2017; Li et al., 2017).

We have carefully estimated speeds and directions of seven individual NLC points in each of these two different layers. The results of this analysis are as follows. For the NLC layer visually moving from the bottom to the top, the average NLC speed was about 28 m/s, with the average azimuth of about 18° (counting clockwise



374 from the north). For the NLC layer moving from the top to the bottom, the average NLC speed was about 60
 375 m/s, with the average azimuth of about 193°. These statistical results are summarized in Table 1 as well as
 376 shown in Fig. 11, demonstrating NLC velocity vectors (green and yellow arrows) estimated for the two different
 377 layers. Note that we have taken into account the velocity vector of the TRANSAT flight (zonal and meridional
 378 speed was -10.5 m/s and -7.1 m/s, respectively) when calculating these NLC wind velocities vectors. To
 379 calculate NLC speeds, the average height of the entire cloud layer was chosen as 83 km. Uncertainty in the
 380 height of the NLC layers between 82 and 86 km gives an error of 3–4% of the average NLC speed.

381 It can be assumed that different movements of the two NLC layers were caused by different wind systems
 382 located at different heights in the mesopause region. We cannot measure the heights of the different NLC layers
 383 but we can consider a model simulation to check this assumption. We utilize JAWARA zonal and meridional
 384 wind data in the mesopause region taken at 06:00 UTC on 25 June 2024, i.e., when and where different motions
 385 of the NLC were observed.

386 JAWARA wind data are shown in Fig. 11 by the vector field as well as by the absolute wind speed (color
 387 code). Panel A represents JAWARA wind data at the pressure level of 0.0042 hPa (~82.9 km) above Greenland
 388 and seven NLC velocity vectors (green arrows) observed in the NLC layer which was moving in the NNE
 389 direction (visually from the bottom to the top). The average wind speed was about 21 m/s in the direction of 13°
 390 (counting clockwise from the north) in the vicinity of the observed NLC. Panel B illustrates JAWARA wind data
 391 at the pressure level of 0.0017 hPa (~86.8 km). One can see about the opposite direction (to SSW) of the model
 392 wind field to that shown on panel A. The average JAWARA wind speed was about 56 m/s, with the average
 393 azimuth of 188°, in the vicinity of the observed NLC. Seven NLC velocity vector are shown by the yellow
 394 arrows which have about the same speed and the direction of motion. All these statistical data are summarized in
 395 Table 1, which demonstrate good agreement between the measured NLC and JAWARA wind velocities both in
 396 the absolute value and in the propagation direction, taking into account their uncertainties. Note that the
 397 JAWARA model has a low horizontal spatial resolution (2.81° or ~310 km in latitude and ~113 km in longitude
 398 in the analyzed space domain over Greenland) and cannot reproduce wave dynamics due to small-scale gravity
 399 waves. However, in this particular case, the JAWARA model does correspond well to the observed motions of
 400 the two different NLC layers.

401

402 **Table 1.** Statistical parameters of the movement of two different layers observed in NLC during the TRANSAT
 403 balloon flight on 25 June 2024. For comparison, wind data from the JAWARA model are shown. Uncertainties
 404 represent one standard deviation.

Two NLC layers oppositely moved in image frame	NLC speed (m/s)	NLC azimuth (degree from north)	JAWARA wind speed (m/s)	JAWARA wind azimuth (degree from north)
From bottom to top	27.8±10.0	18.2±8.2	21.0±3.7 at 0.0042 hPa	13.0±12.0 at 0.0042 hPa
From top to bottom	60.5±11.3	192.5±2.2	56.1±2.5 at 0.0017 hPa	188.0±4.3 at 0.0017 hPa

405

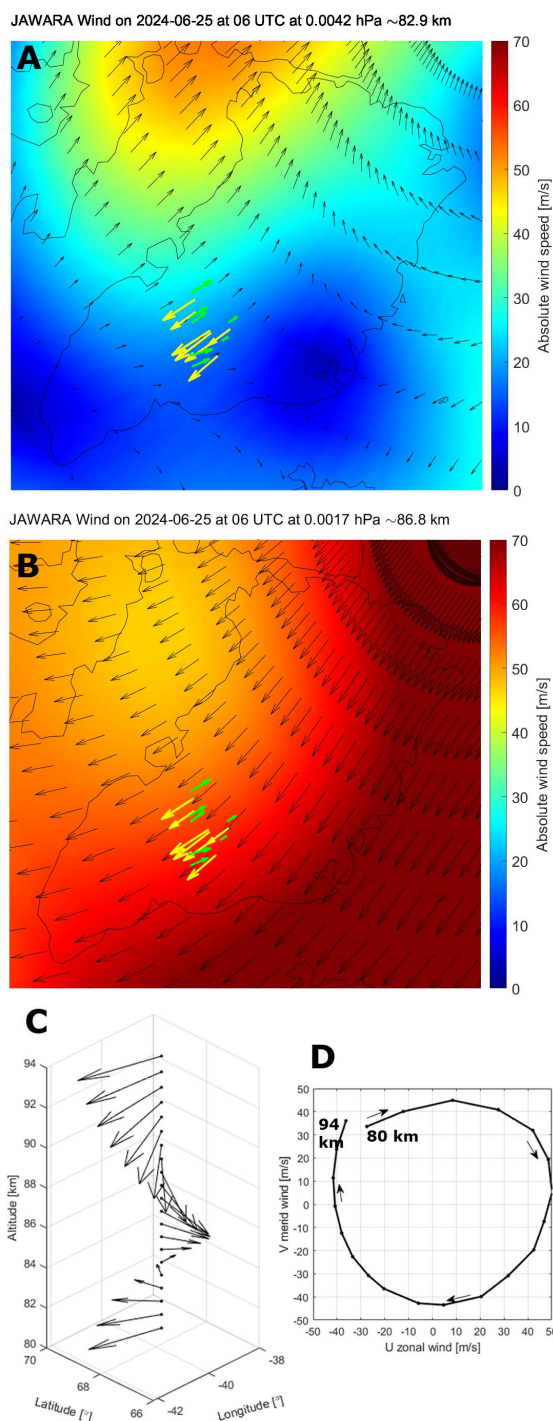
406 Panel C of Fig. 11 shows the JAWARA wind velocity vector as a function of altitude for a specific point in
 407 the vicinity of the observed NLC. The cyclic rotation of the wind velocity vector is clearly seen between 80 and
 408 94 km altitude, i.e., there was a circular rotation of the wind vector along the azimuth of 360°. Panel D illustrates



the corresponding hodograph of the tip of the horizontal wind vector with the subtracted mean velocity values (-33 m/s and -18 m/s for the zonal and meridional wind component, respectively) between 80 and 94 km, that is, perturbations of the horizontal wind velocity. It is well known that a gravity wave induces horizontal wind variations rotating, in general, elliptically with height, and hodograph analysis is commonly used to derive gravity wave parameters (Gossard and Hooke, 1975; Eckermann, 1996 and references therein). In the present case, the hodograph has an almost circular form, implying near circular polarization ($P \approx 0$). Perturbations of the horizontal wind are of 45-50 m/s, and the perturbation vector has a clockwise rotation with increasing height which means that the group velocity of this particular gravity wave was propagating upward (phase velocity was downward). Such an inertia-gravity wave could indeed generate winds in different directions in the given volume of the mesopause, forming a multiple-layer structure from a single NLC layer. The inertia-gravity wave interpretation is a plausible scenario which is consistent with JAWARA winds and NLC motions. At the same time, it should be noted that the background wind in the mesopause region abruptly changes its speed and direction with altitude in summer (Portnyagin and Solovjova, 2000; Conte et al., 2025). Therefore, other mechanisms such as the vertical displacement of the NLC layer by gravity waves, may provide the observed different NLC motions.

It is important to note the following. The clockwise wind rotation with altitude by JAWARA was the opposite of that found by Conte et al. (2025), who have analyzed long-term meteor radar measurements in the mesopause region at high latitudes over northern Norway. The authors have obtained the counter-clockwise rotation of the mean wind speed with altitude in the summer time. The same effect of the wind rotation with altitude is predicted by the global empirical wind model for the upper mesosphere/lower thermosphere (Portnyagin and Solovjova, 2000). In this present case, the clockwise rotation of the wind speed indicates the dominance of the inertia-gravity wave over the mean wind rotation speed in the space-time domain under consideration. Also, we should note that even without inertia-gravity waves, winds in the mesopause region can rotate with altitude (Ekman spiral) under the action of the Ekman-type mechanism involving Coriolis force and turbulent viscosity (Chkhetiani and Shalimov, 2010; 2022).

434



435

436

437

Figure 11: JAWARA wind data (thin black arrows) at the pressure level of 0.0042 hPa, ~82.9 km (A) and at the pressure level of 0.0017 hPa, ~86.8 km (B) at 06 UTC on 25 June 2024. The color code is the absolute horizontal



438 wind speed. The green and yellow arrows show velocities of NLC moving in opposite directions (see the text).
 439 (C) JAWARA wind velocity vector selected for a specific location (68.4°N, 39.4°W) as a function of altitude
 440 between 80 and 94 km. (D) Hodograph of disturbances of the horizontal wind velocity vector between 80 and 94
 441 km. The thin arrows show the direction (clockwise rotation) of wind velocity disturbances with altitude.

442

443 **5 Conclusions**

444 Observations of noctilucent clouds were performed from the stratosphere during the TRANSAT transatlantic
 445 long-duration balloon flight between Sweden and Canada on 22-26 June 2024. NLC were observed with the
 446 SONC imager composed of three high-resolution SONY $\alpha 7$ Mark III cameras, stabilized on the TRANSAT
 447 gondola. NLC cannot be detected by an imager from the ground during the midnight Sun season due to strong
 448 background scattering in the lower atmosphere. However, an observation from the stratosphere can detect NLC
 449 during 24 hours. These measurements offer an unprecedented view of mesospheric cloud dynamics on small-
 450 and large-scales, bridging the observational gap between ground-based and satellite platforms. The main results
 451 of this study can be summarized as follows:

- 452 1. One wide-angle camera was completely operational during the whole flight for 3.8 days, taking a total of
 453 40,000 images, of which about 6200 images are suitable for scientific analysis.
- 454 2. NLC were detected nearly continuously during the whole flight, showing a strong variability in space and
 455 time. The dominant role of solar thermal tides in the summer mesopause decreases when NLC are observed
 456 on large scales of about 1500 km. At such scales, gravity waves of various scales from 1 to several hundred
 457 km play the largest role, evolving and modulating NLC layers in different regions of the polar mesopause.
 458 Note that this result was obtained on the basis of a single 3.8-day flight and a limited range of latitudes (60-
 459 75°N) and longitudes (45°E-95°W). Thus, the present case study cannot claim to be a general statement
 460 about the relative importance of solar tides compared to gravity waves.
- 461 3. Ground-based support of the TRANSAT balloon campaign was represented by two lidars located at Esrange
 462 and Andoya. Both lidars registered NLC at the time of the initial phase of the balloon flight over northern
 463 Scandinavia. The NLC layered was continuous from 20 UTC on 22 June until 09 UTC on 23 June,
 464 modulated in height between 81 and 86 km, and showing a double-layer structure.
- 465 4. The same mesospheric cloud layer was recorded from the stratosphere and space around noon on 25 June
 466 2024. Such a simultaneous common-volume NLC detection was carried out, for the first time, using a limb-
 467 geometry by the MATS satellite. The extended cloud layer was observed over at least Greenland, Baffin Bay
 468 and Baffin Island, with part of this layer registered from the stratosphere over the west coast of Greenland
 469 and Baffin Bay. Images from the stratosphere showed complex wave dynamics, with interference of small-
 470 scale waves and turbulent regions below what MATS can partly resolve. Therefore, observations of clouds
 471 from the stratosphere and space, using limb geometry, complement each other well.
- 472 5. Gravity waves had characteristic horizontal wavelengths of 30-40 km for the case study considered in the
 473 mesopause over Greenland on 25 June 2024.
- 474 6. One peculiar case of the NLC disappearance in the polar mesopause in the afternoon of 24 June 2024 has
 475 been analyzed. This cloud disappearance was caused by the localized warm spot in the mesopause region
 476 between Greenland and Scandinavia, as shown by Aura/MLS satellite and JAWARA model data. This warm
 477 spot in the mesopause region was caused by the intrusion of a warm air mass from middle to high latitudes.



7. Different movements of NLC were observed in the morning of 25 June 2024 over Greenland. One part of the clouds moved to NNE, another one moved to SSW. A detailed analysis of wind data based on the JAWARA model showed that there were different wind systems between 80 and 94 km altitude over Greenland, with a clockwise wind rotation with altitude. Most likely, a large inertia-gravity wave propagated upwards, causing significant disturbances (45-50 m/s) of the horizontal wind. The wind disturbances caused NLC to move differently at different altitudes. Other mechanisms such as the vertical displacement of the NLC layer by gravity waves may explain the observed different NLC motions.

These results demonstrate the scientific value of long-duration stratospheric balloon missions for mesospheric research. Future campaigns of this type will benefit from expanded multi-spectral imaging, real-time data transmission, and coordinated ground-satellite observations to further improve understanding of mesospheric cloud dynamics. A statistical analysis of the wave dynamics observed in NLC during the 2024 TRANSAT balloon flight, and investigation of microphysical properties of NLC ice particles will be addressed in future studies.

491

492 **Data availability**

Two video files of the SONC experiment are available on the Harvard Dataverse repository (<https://doi.org/10.7910/DVN/AKJK4P>; <https://doi.org/10.7910/DVN/1PHRZU>). Individual NLC images taken from the stratosphere by the SONC experiment that support the findings of this study are available at the HEMERA Data Centre (<https://data.hemera-h2020.eu/atmospheric-balloon-experiments/#/>) as well as will be made available on request.

498

499 **Author contributions**

PD, HS, NP, VP, JK and AR have designed two balloon-borne experiments dedicated to studies of noctilucent clouds and infrasound waves. PD wrote the draft of the paper and made analyses of the SONC images, Esrange lidar, Aura/MLS and JAWARA data. LM made analysis of the MATS satellite data. PV and JH performed Esrange lidar measurements. GB performed ALOMAR lidar measurements. DE designed and produced the electric control unit for the SONC imager. All authors discussed the results and contributed to revisions of the text and the figures.

506

507 **Competing interests**

The contact author has declared that none of the authors has any competing interests.

509

510 **Acknowledgments**

The authors thank the CNES/INSU-CNRS Balloon Programme. The TRANSAT balloon flight was funded and performed by the French Space Agency (CNES). The authors thank the Aura/MLS team for providing temperature and water vapor data around the globe during the 2024 TRANSAT balloon flight.

514

515 **Financial support**

The SONC imager hardware (imager and electronic control unit) was funded by the Kempe Foundation (Kempe Stiftelsen) under grant agreement JCK-1901.4. The infrasound instrument and flight costs of the SONC

517



518 and infrasound instruments were financed under research grant 42/17 from the Swedish National Space Agency
 519 (Rymdstyrelsen). The MATS satellite and JH were financed by the Swedish National Space Agency under grant
 520 2021-00052. LM was financed by the Swedish National Space Agency under grant 2022-00108 and the Swedish
 521 Research Council (Vetenskapsrådet) under grant 2021-04876.

522

523 References

524 Bailey, S. M., Thomas, G. E., Rusch, D. W., Merkel, A. W., Jeppesen, C., Carstens, J. N., Randall, C. E.,
 525 McClintock, W. E., and Russell, J. M.: Phase functions of polar mesospheric cloud ice as observed by the CIPS
 526 instrument on the AIM satellite, *J. Atmos. Sol. Terr. Phys.* 71, 3-4, 373–380.
 527 <http://dx.doi.org/10.1016/j.jastp.2008.09.039>, 2009.

528 Baumgarten, G., and Fritts, D. C.: Quantifying Kelvin-Helmholtz instability dynamics observed in
 529 noctilucent clouds: 1. Methods and observations, *J. Geophys. Res. Atmos.*, 119, 9324–9337,
 530 doi:10.1002/2014JD021832, 2014.

531 Baumgarten, G., Chandran, A., Fiedler, J., Hoffmann, P., Kaifler, N., Lumpe, J., Merkel, A., Randall, C. E.,
 532 Rusch, D., and Thomas, G.: On the horizontal and temporal structure of noctilucent clouds as observed by
 533 satellite and lidar at ALOMAR (69N), *Geophys. Res. Lett.*, 39, L01803, doi:10.1029/2011GL049935, 2012.

534 Baumgarten, G.: Doppler Rayleigh/Mie/Raman lidar for wind and temperature measurements in the middle
 535 atmosphere up to 80 km, *Atmos. Meas. Tech.*, 3, 1509-1518. doi:10.5194/amt-3-1509-2010, 2010.

536 Baumgarten, G., Fiedler, J., Fricke, K. H., Gerding, M., Hervig, M., Hoffmann, P., et al.: The noctilucent
 537 cloud (NLC) display during the ECOMA/MASS sounding rocket flights on 3 August 2007: morphology on
 538 global to local scales, *Ann. Geophys.*, 27, 953–965, 2009.

539 Blum, U., and Fricke, K. H.: The Bonn University lidar at the Esrange: technical description and capabilities
 540 for atmospheric research, *Ann. Geophys.*, 23, 1645–1658, 2005.

541 Chkhietiani, O., and Shalimov, S.: On anomalous wind amplitudes in the lower ionosphere, *J. Atmos. Sol.-*
 542 *Terr. Phys.*, 240, 105960, <https://doi.org/10.1016/j.jastp.2022.105960>, 2022.

543 Chkhietiani, O. G., and Shalimov, S. L.: Helicity in the upper atmosphere and Ekman-type instabilities, *Dokl.*
 544 *Earth Sc.*, 431, 345–350, <https://doi.org/10.1134/S1028334X10030177>, 2010.

545 Conte, J. F., Chau, J. L., Renkowitz, T., Latteck, R., Tsutsumi, M., Jacobi, C., Gulbrandsen, N., and Nozawa,
 546 S.: Observing mesoscale dynamics with multistatic specular meteor radars: first climatology of momentum flux,
 547 horizontal divergence and relative vorticity over northern central Europe, *Ann. Geophys.*, 43, 603–619,
 548 <https://doi.org/10.5194/angeo-43-603-2025>, 2025.

549 Dalin, P., Suzuki, H., Pertsev, N., Perminov, V., Efremov, D., Voelger, P., Narayanan, V. L., Mann, I.,
 550 Häggström, I., Zalcik, M., Ugonnikov, O., Hedin, J., Gumbel, J., Latteck, R., and Baumgarten, G.: Studies of
 551 noctilucent clouds from the stratosphere during the SONC balloon-borne experiment in 2021. *J. Atmos. Sol.-*
 552 *Terr. Phys.*, 240, 105959, doi.org/10.1016/j.jastp.2022.105959, 2022.

553 Dalin, P., Pertsev, N., Perminov, V., Efremov, D., and Romejko, V.: Stratospheric observations of
 554 noctilucent clouds: a new approach in studying middle- and large-scale mesospheric dynamics, *Ann. Geophys.*,
 555 38, 61–71, <https://doi.org/10.5194/angeo-38-61-2020>, 2020.

556 Dalin, P., Pertsev, N., Perminov, V., Efremov, D., and Romejko, V.: Looking at “night-shining” clouds from
 557 the stratosphere, *Eos–AGU*, 100, <https://doi.org/10.1029/2019EO118439>, 2019.



- 558 Dalin, P., Pogoreltsev, A., Pertsev, N., Perminov, V., Shevchuk, N., Dubietis, A., Zalcik, M., et al.: Evidence
559 of the formation of noctilucent clouds due to propagation of an isolated gravity wave caused by a tropospheric
560 occluded front, *Geophys. Res. Lett.*, 42, 2037–2046, <https://doi.org/10.1002/2014GL062776>, 2015.
- 561 Dalin, P., Pertsev, N., Frandsen, S., Hansen, O., Andersen, H., Dubietis, A., and Balciunas, R.: A case study
562 of the evolution of a Kelvin-Helmholtz wave and turbulence in noctilucent clouds, *J. Atmos. Sol.-Terr. Phys.*,
563 72, 14–15, 1129–1138, doi:10.1016/j.jastp.2010.06.011, 2010.
- 564 Dalin, P., Pertsev, N., Zadorozhny, A., Connors, M., Schofield, I., Shelton, I., et al.: Ground-based
565 observations of noctilucent clouds with a northern hemisphere network of automated digital cameras, *J. Atmos.*
566 *Sol.-Terr. Phys.*, 70, 1460–1472, 2008.
- 567 DeLand, M. T., and Thomas, G. E.: Updated PMC trends derived from SBUV data, *J. Geophys. Res. Atmos.*,
568 120, 2140–2166, doi:10.1002/2014JD022253, 2015.
- 569 Demissie, T. D., Espy, P. J., Kleinknecht, N. H., Hatlen, M., Kaifler, N., and Baumgarten, G.: Characteristics
570 and sources of gravity waves observed in noctilucent cloud over Norway, *Atmos. Chem. Phys.*, 14, 12133–
571 12142, doi:10.5194/acp-14-12133-2014, 2014.
- 572 Dubinskii, A. Yu., and Popel, S. I.: Formation and evolution of dusty plasma structures in the ionosphere,
573 *JETP Lett.*, 96, 21–26, doi:10.1134/S0021364012130048, 2012.
- 574 Eckermann, S. D.: Hodographic analysis of gravity waves: relationships among Stokes parameters, rotary
575 spectra and cross-spectral methods, *J. Geophys. Res.*, 101, 19169–19174, 1996.
- 576 Fiedler, J., Baumgarten, G., Berger, U., Hoffmann, P., Kaifler, N., and Lübken, F.-J.: NLC and the
577 background atmosphere above ALOMAR, *Atmos. Chem. Phys.*, 11, 5701–5717. doi:10.5194/acp-11-5701-2011,
578 2011.
- 579 Fritts, D. C., Miller, A. D., Kjellstrand, C. B., Geach, C., Williams, B. P., Kaifler, B., et al.: PMC Turbo:
580 Studying gravity wave and instability dynamics in the summer mesosphere using polar mesospheric cloud
581 imaging and profiling from a stratospheric balloon, *J. Geophys. Res. Atmos.*, 124, 6423–6443.
582 <https://doi.org/10.1029/2019JD030298>, 2019.
- 583 Froidevaux, L., Livesey, N. J., Read, W. G., Jiang, Y. B., Jiménez, C. C., Filipiak, M. J., Schwartz, M. J., et
584 al.: Early validation analyses of atmospheric profiles from EOS MLS on the Aura satellite, *IEEE Transactions on*
585 *Geoscience and Remote Sensing*, 44, 5, 1106–1121, 2006.
- 586 Gadsden, M., and Schröder, W.: *Noctilucent Clouds*, Springer, New York, 1989.
- 587 Gao, H., Shepherd, G. G., Tang, Y., Bu, L., and Wang, Z.: Double-layer structure in polar mesospheric
588 clouds observed from SOFIE/AIM, *Ann. Geophys.*, 35, 295–309, <https://doi.org/10.5194/angeo-35-295-2017>,
589 2017.
- 590 Gossard, E. E., and Hooke, W. H.: *Waves in the atmosphere: atmospheric infrasound and gravity waves –*
591 *their generation and propagation*, Elsevier Scientific Publishing Co, Amsterdam, 1975.
- 592 Gumbel, J., Megner, L., Christensen, O. M., Ivchenko, N., Murtagh, D. P., Chang, S., Dillner, J., Ekebrand, T.,
593 Giono, G., Hammar, A., Hedin, J., et al.: The MATS satellite mission – gravity wave studies by Mesospheric
594 Airglow/Aerosol Tomography and Spectroscopy, *Atmos. Chem. Phys.*, 20, 431–455, [https://doi.org/10.5194/acp-](https://doi.org/10.5194/acp-20-431-2020)
595 [20-431-2020](https://doi.org/10.5194/acp-20-431-2020), 2020.
- 596 Gumbel, J., and Witt, G.: Rocket-borne photometry of NLC particle populations, *Adv. Space Res.*, 28, 7, 1053–
597 1058, 2001.



- 598 Kaifler, N., Baumgarten, G., Klekociuk, A. R., Alexander, S. P., Fiedler, J., and Lübken, F.-J.: Small scale
599 structures of NLC observed by lidar at 69°N/69°S and their possible relation to gravity waves, *J. Atmos. Sol.-*
600 *Terr. Phys.*, 104, 244–252, doi:10.1016/j.jastp.2013.01.004, 2013.
- 601 Karlsson, B., and Gumbel, J.: Challenges in the limb retrieval of noctilucent cloud properties from
602 Odin/OSIRIS, *Adv. Space Res.*, 36, 935–942, doi:10.1016/j.asr.2005.04.074, 2005.
- 603 Koshin, D., Sato, K., Miyazaki, K., and Watanabe, S.: An ensemble Kalman filter data assimilation system
604 for the whole neutral atmosphere, *Geosci. Model Dev.*, 13, 3145–3177, [https://doi.org/10.5194/gmd-13-3145-](https://doi.org/10.5194/gmd-13-3145-2020)
605 2020, 2020.
- 606 Koshin, D., Sato, K., Kohma, M., and Watanabe, S.: An update on the 4D-LETKF data assimilation system
607 for the whole neutral atmosphere, *Geosci. Model Dev.*, 15, 2293–2307, [https://doi.org/10.5194/gmd-15-2293-](https://doi.org/10.5194/gmd-15-2293-2022)
608 2022, 2022.
- 609 Koshin, D., Sato, K., Watanabe, S., et al.: The JAGUAR-DAS whole neutral atmosphere reanalysis:
610 JAWARA, *Prog. Earth Planet. Sci.*, 12, 1, <https://doi.org/10.1186/s40645-024-00674-3>, 2025.
- 611 Lambert, A., Read, W. G., Livesey, N. J., Santee, M. L., Manney, G. L., Froidevaux, L., Wu, D. L.,
612 Schwartz, M. J., Pumphrey, H. C., Jimenez, C., Nedoluha, G. E., et al.: Validation of the Aura Microwave Limb
613 Sounder middle atmosphere water vapor and nitrous oxide measurements, *J. Geophys. Res.*, 112, D24S36, 2007.
- 614 Li, H., Wu, J., and Zhou, Z.: The formation of multiple layers of ice particles in the polar summer mesopause
615 region, *Ann. Geophys.*, 34, 117–122, doi:10.5194/angeo-34-117-2016, 2016.
- 616 Liu, X., Yue, J., Xu, J., Yuan, W., Russell III, J. M., Hervig, M. E., and Nakamura, T.: Persistent longitudinal
617 variations in 8 years of CIPS/AIM polar mesospheric clouds, *J. Geophys. Res. Atmos.*, 121, 8390–8409,
618 doi:10.1002/2015JD024624, 2016.
- 619 Megner, L., Gumbel, J., Christensen, O. M., Linder, B., Murtagh, D., Ivchenko, N., Krasauskas, L., Hedin, J.,
620 Dillner, J., and Stegman, J.: MATS satellite images (level 1b) of airglow and noctilucent clouds in the
621 mesosphere/lower thermosphere, February–May 2023, Dataset version 1.0, Bolin Centre Database,
622 <https://doi.org/10.17043/mats-level-1b-limb-cropd-1.0>, 2025.
- 623 Miller, A. D., Fritts, D. C., Chapman, D., Jones, G., Limon, M., Araujo, D., et al.: Stratospheric imaging of
624 polar mesospheric clouds: a new window on small-scale atmospheric dynamics, *Geophys. Res. Lett.*, 42, 6058–
625 6065, doi:10.1002/2015GL064758, 2015.
- 626 Murphy, D. M., and Koop, T.: Review of the vapour pressures of ice and supercooled water for atmospheric
627 applications, *Q. J. R. Meteorol. Soc.*, 131, 1539–1565. doi:10.1256/qj.04.94, 2005.
- 628 Pautet, P.-D., Stegman, J., Wrasse, C. M., Nielsen, K., Takahashi, H., Taylor, M. J., et al.: Analysis of gravity
629 waves structures visible in noctilucent cloud images, *J. Atmos. Sol.-Terr. Phys.*, 73, 14–15, 2082–2090, doi:
630 10.1016/j.jastp.2010.06.001, 2011.
- 631 Pertsev, N. N., Dalin, P. A., Perminov, V. I., Gusev, N. K., Tsimerinov, E. Yu., Solodovnik, A. A.,
632 Zadorozhny, A. M., Korotyshkin, D. V., and Bordonskiy, G. S.: Analysis of noctilucent cloud fields according to
633 ground-based network and airborne photography data, *Izv. Atmos. Ocean. Phys.*, 60, 2, 187–194,
634 doi:10.1134/S0001433824700191, 2024.
- 635 Portnyagin, Y. I. and Solovjova, T. V.: Global empirical wind model for the upper mesosphere/lower
636 thermosphere. I. Prevailing wind, *Ann. Geophys.*, 18, 300–315, <https://doi.org/10.1007/s00585-000-0300-y>,
637 2000.



- 638 Rapp, M., Lubken, F.-J., Müllemann, A., Thomas, G. E., and Jensen, E. J.: Small-scale temperature
639 variations in the vicinity of NLC: Experimental and model results, *J. Geophys. Res.*, 107, D19, 4392,
640 doi:[10.1029/2001JD001241](https://doi.org/10.1029/2001JD001241), 2002.
- 641 Read, W. G., Lambert, A., Bacmeister, J., Cofield, R. E., Christensen, L. E., Cuddy, D. T., Daffer, W. H.,
642 Drouin, B. J., Fetzer, E., Froidevaux, et al.: Aura Microwave Limb Sounder upper tropospheric and lower
643 stratospheric H₂O and relative humidity with respect to ice validation, *J. Geophys. Res.*, 112, D24S35, 2007.
- 644 Reimuller, J. D., Thayer, J. P., Baumgarten, G., Chandran, A., Hulley, B., Rusch, D., Nielsen, K., and
645 Lumpe, J.: Synchronized imagery of noctilucent clouds at the day-night terminator using airborne and
646 spaceborne platforms, *J. Atmos. Sol.-Terr. Phys.*, 73, 14-15, 2091-2096, 2011.
- 647 Schwartz, M. J., Lambert, A., Manney, G. L., Read, W. G., Livesey, N. J., Froidevaux, L., Ao, C. O.,
648 Bernath, P. F., Boone, C. D., Cofield, R. E., et al.: Validation of the Aura Microwave Limb Sounder temperature
649 and geopotential height measurements, *J. Geophys. Res.*, 113, D15S11, 2008.
- 650 Suzuki, H., Matsumoto, A., Dalin, P., Nakamura, Y., Ishii, S., Sakanoi, K., Sakaguchi, K., Takada, T., Tsuda,
651 T. T., and Hozumi, Y.: Capability of airline jets as an observation platform for noctilucent clouds at middle
652 latitudes, *Prog. Earth Planet. Sci.*, 9, 11, <https://doi.org/10.1186/s40645-022-00469-4>, 2022.
- 653 Thomas, G.E.: Solar Mesosphere Explorer measurements of polar mesospheric clouds (noctilucent clouds), *J.*
654 *Atmos. Terr. Phys.*, 46, 9, 819-824, 1984.
- 655 Tsuda, T. T., Hozumi, Y., Kawaura, K., Tatsuzawa, K., Ando, Y., Hosokawa, K., et al.: Detection of polar
656 mesospheric clouds utilizing Himawari-8/AHI full-disk images, *Earth Space Sci.*, 9,
657 2021EA002076, <https://doi.org/10.1029/2021EA002076>, 2022.
- 658 Wallis, S., DeLand, M., and Savigny, C.: Did the 2022 Hunga eruption impact the noctilucent cloud season in
659 2023/24 and 2024?, *Atmos. Chem. Phys.*, 25, 3635–3645. <https://doi.org/10.5194/acp-25-3635-2025>, 2025.
- 660 Zadorozhny, A. M., Tyutin, A. A., Witt, G., Wilhelm, N., Wälchli, U., Cho, J. Y. N., and Swartz, W. E.:
661 Electric field measurements in the vicinity of noctilucent clouds and PMSE, *Geophys. Res. Lett.*, 20, 20, 2299-
662 2302, 1993.